Pore-Resolving Simulations to Study the Impacts of Char Morphology on Zone II Combustion and Effectiveness Factor Models

Dongyu Liang
Marquette University

Simcha L. Singer
Marquette University, simcha.singer@marquette.edu

Pore-Resolving Simulations to Study the Impacts of Char Morphology on Zone II Combustion and Effectiveness Factor Models

Dongyu Liang
Department of Mechanical Engineering, Marquette University, Milwaukee, WI
Simcha Singer
Department of Mechanical Engineering, Marquette University, Milwaukee, WI

Abstract

Combustion and gasification of pulverized char often occur under zone II conditions, in which the rate of conversion depends on both heterogeneous reaction and gas transport within the particle's porous structure. The morphology of porous char has a strong influence on intra-particle diffusion, and thus, on the overall conversion rate. Because pulverized coal and biomass char particles are often irregularly shaped and contain pores and voids which can approach the size of the particles themselves, conventional models based on spherical symmetry and coarse-grained, upscaled, effective continuum conservation equations are not applicable or appropriate. A recent 3-D, pore-resolving CFD simulation approach based on real char particle

geometries obtained from X-ray micro-computed tomography (micro-CT) obviates the need to upscale over large heterogeneities and to make oversimplifying geometric assumptions. The micro-CT-based pore-resolving approach is employed here to study zone II combustion for fifty pulverized, porous coal char particles produced at a high heating rate. The large pores often present in char particles enhance reactant transport throughout the particles, even within the micro- and meso-porous carbon surrounding the large pores. This is particularly the case for network-type particle structures, due to the prominence of channels that extend from the particle surface. Because reactor-scale codes often employ one-dimensional models to calculate the reaction rates of tracked particles, pore-resolving simulations are used to assess the accuracy of existing effectiveness factor models for real char. Cenospherical particles can be reasonably modeled using an effectiveness factor solution for hollow spheres, but the behavior of more complex network morphologies is not well-predicted by any of the effectiveness factor models examined.

Keywords
Pore-scale simulation, Char combustion, Micro-CT, Effectiveness Factor, Upscaling

1. Introduction

During combustion and gasification of solid fuels like coal and biomass, porous char particles are formed in-situ during devolatilization. Because char conversion occurs more slowly than devolatilization and volatile combustion, it represents the overall rate-limiting step. For combustion and high-temperature gasification of pulverized coal and biomass, the char particles typically react under zone II conditions [1], [2], [3], [4], [5], [6], in which heterogeneous reaction and gas diffusion both impact the overall rate of char consumption. The coupling between reaction and diffusion at the particle-scale can affect outputs at the reactor-scale, such as carbon conversion and temperature [7,8]. Furthermore, reactor-scale computational fluid dynamics (CFD) simulations, which are used to optimize boiler and gasifier design and operating conditions, are sensitive to submodels used for individual particles [7], [8], [9], [10], [11]. The fidelity of CFD codes for solid fuel combustion and gasification therefore depends on the accuracy of the submodels for char conversion, which, in turn, requires a fundamental understanding of the interplay between transport, reaction and morphology at the particle-scale [8,[12], [13], [14].

Due to the innumerable pores in most coal and biomass char particles, physics and chemistry at the pore-scale must be "upscaled" [15,16] to transform conservation equations for the actual pore space into "effective-continuum" conservation equations for smoothly varying variables. The validity of the effective-continuum approach requires a separation of length scales; the upscaling must be performed over representative volume elements large enough to contain a statistical number of heterogeneities (pores), but small enough to resolve particle-scale gradients. This implies that the characteristic size of the pores be much smaller than: (a) the size of the particle itself, and (b) the characteristic length of the physical processes to be resolved [17,18]. However, char particles produced from many coal and biomass feedstock contain a range of pore sizes, including large macro-pores and voids that can approach the size of the particles themselves, leading to violation of the upscaling constraints [17,19].

Nonetheless, most char consumption models assume, explicitly or implicitly, that particles are amenable to treatment as volume-averaged spheres or cylinders, with smoothly varying effective properties and sub-grid-scale porosity. This is the case for stand-alone, spatially resolved models that examine the impacts of reaction, advection and diffusion on density/diameter evolution [20], [21], [22], including those that explicitly attempt to account for the presence of large pores [23], as well as effectiveness factor models used in reactor-scale CFD codes. Application of effective-continuum models in the absence of scale separation can lead to inaccurate predictions of heterogeneous reactions [24], mixing [25] and hotspots [26]. Experiments have

demonstrated that real char particles cannot be accurately modeled as homogeneous, porous spheres [14] and that char morphology has a strong impact on conversion for zone II conditions [12,14].

Some studies have used discrete networks to model char consumption [17,19,27,28], but the ability of such networks to emulate real char morphology is unconfirmed and the approach is difficult to combine with other physics. Others have modeled reaction and transport in char particles using resolved, but idealized, voids. For instance, confocal scanning laser microscopy was used to obtain the morphological characteristics of biomass particles [29] which were then used to generate idealized geometries for non-reacting simulations of heat and mass transfer [29,30]. Comparison of the resolved model to an effective-continuum model demonstrated the inability of the latter to accurately simulate both heat and mass transfer [29]. Oxy-combustion of a porous coal char particle has also been modeled using resolved, but idealized, voids, by treating a single particle as an agglomerate of smaller, non-porous spheres [31]. A similar, single particle study of coal char oxy-combustion used idealized, resolved cone-shaped pores [32]. Man-made catalyst particles, which often contain geometrically regular pores, are more amenable to treatments using idealized, resolved voids. For instance, reaction and transport in porous catalyst particles was studied using resolved cylindrical holes while the surrounding grains were treated as an effective-continuum [33], [34], [35], [36].

An alternative approach to modeling reaction and transport in disordered porous char while respecting the length-scale constraints is to experimentally obtain the real particle morphology in three dimensions (3-D) and to perform pore-resolving simulations. X-ray micro-computed tomography (micro-CT) is an attractive technique for obtaining the internal and external geometry of disordered porous particles [37]. Recently, in-situ micro-CT was used to image the evolution of density and temperature in large (~19 mm), smoldering biomass particles [38]. Scans were acquired every 90 s with a voxel size of 135 µm, and demonstrated the importance of biomass structure on the oxidation process [38]. Micro-CT (voxel size 2 µm) was also used in conjunction with zone II experiments to demonstrate the impact of the large pore (> 5 µm) morphology, and the enhanced reactant transport therein, on biomass char structure evolution [39]. Non-reacting simulations of transport in coal macropores and voids larger than 13.85 µm based on geometries obtained from micro-CT [40] have also been reported.

The first realistic, pore-resolving, reacting flow simulation for char particle conversion was developed [41] to address the violation of the length-scale constraints by effective-continuum models. An 850 µm coal char particle was imaged in three dimensions using micro-CT (voxel size 20 µm). The particle was then isotropically scaled to 100 µm to represent pulverized char and was meshed and exported for CFD simulation under entrained flow gasification conditions. Conservation equations based on first principles were applied within the resolved large pores, which could not be included in the effective-continuum due to their violation of the length-scale constraints for upscaling. For the regions of "microporous" char that surround the large voids, effective-continuum equations were employed, since they contain smaller pores amenable to upscaling. The simulation was compared to an effective-continuum simulation of a spherical char particle with identical initial mass, volume, porosity, surface area and equivalent diameter. The oxygen penetration and rates of conversion differed significantly between the two models before the gasification transitioned from zone II to zone I conditions [41].

In this paper, the micro-CT-based, pore-resolving simulation approach [41]is extended to a larger distribution of particles, with smaller sizes (~100 µm), reacting in a combustion environment. Pore-resolving simulations are used to study a population of 50 pulverized, bituminous coal char particles [42] formed at high heating rate, whose 3-D internal and external geometries have been obtained from high resolution micro-CT. The simulations are used to assess the fidelity of existing one-dimensional effectiveness factor models, which are amenable to incorporation in reactor-scale CFD codes. In Section 2, the methods used to produce the char particles and to obtain the internal and external particle morphologies using high-resolution micro-CT are presented. An

overview of the pore resolving CFD simulation [41]and the calculation of effectiveness factors from the 3-D data is provided. The methods for calculating effectiveness factors from several 1-D models are then discussed, focusing on the geometric parameters obtained from micro-CT imaging of the real particles. In Section 3, results from the pore-resolving simulations are used to examine the impacts of morphology on reactant transport, and effectiveness factors for real char geometries are compared to predictions of 1-D models proposed in the literature. Finally, conclusions are drawn in Section 4.

2. Methods and models

2.1. Char production

Bituminous coal particles (Illinois #6) were sieved to a 105 μm nominal diameter. The coal contained 46.61% fixed carbon, 40.34% volatile matter and 13.05% ash on a dry basis, and was composed of 67.48% carbon, 4.82% hydrogen, 8.60% oxygen, 1.53% nitrogen and 4.52% sulfur on a dry, ash-free basis. The particles were scattered in a single layer on a sheet of aluminum foil, covered with a glass beaker, filled with argon, and sealed. The inverted beaker was then placed in a pre-heated, 800 °C muffle oven for 30 s, resulting in a maximum heating rate estimated to approach 10,000 K/s.

2.2. Micro-CT imaging and image processing

Dozens of char particles were attached to a micro-pipette tip and imaged using a GE v|tome|x s 240 X-ray micro-CT scanner operating at 80 kV and 130 μA, with a voxel size of 1.632 μm. The stack of reconstructed TIFF images was then imported into the ScanIP (Synopsys, Mountain View, USA) software for processing, segmentation, and meshing. Individual particles were segmented from one another and from the pipette support material. A recursive Gaussian filter was initially applied to the greyscale images of the individual particles, which were then segmented into what is termed the "microporous solid" and "resolved voids/pores" using manual gray-scale thresholding. The microporous solid region is comprised of unresolved micropores, mesopores and macropores, as well as carbonaceous char. The distribution of particles was comprised of cenospheres (particles with a large central void) and network-type particles with a more complex pore structure [43]. Most of the cenospheres could be classified as thick-walled crassispheres rather than thin-walled tenuispheres. Three dimensional renderings of a cenospherical particle, a transitional particle and a more complex particle structure, after filtering and segmentation, are shown in Fig. 1, indicating the resolved pores and voids and the microporous char.
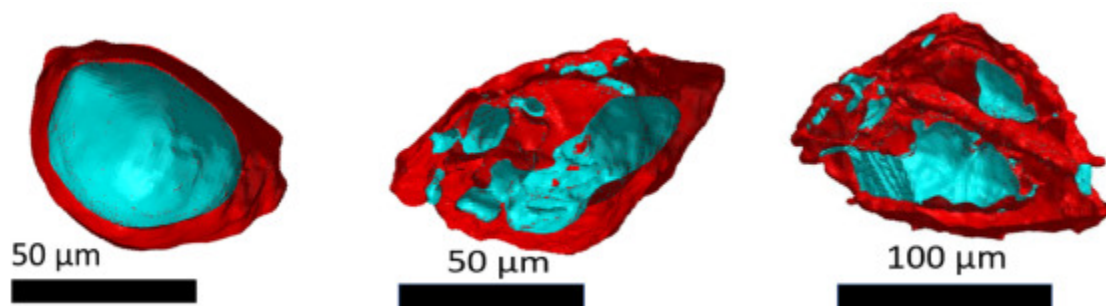

Fig. 1. Three-dimensional renderings of three char particles, with the resolved pores/voids shown in blue and the microporous solid in red for cenosphere (left), transitional (middle), and network (right) particles. (For interpretation of the references to color in this figure caption, the reader is referred to the web version of this article.)

2.3. Pore-resolving CFD simulation

The pore-resolving simulation has been described in detail previously [41], but is summarized here. To focus on the impacts of particle morphology on the reaction-transport balance, the effective particle diameter and the total particle volume were made identical for every particle by using the isotropic scaling factor

(1)

$$R_{scale} = \frac{\left(\frac{6}{\pi}\left(V_{mps} + V_{voids}\right)\right)^{\frac{1}{3}}}{100\mu m}$$

where V_{mps} is the volume of microporous solid and V_{voids} is the volume of the resolved pores and voids, which were calculated using volume integration of the 3-D geometries obtained from micro-CT imaging (see Table S1 in the Supplementary Material). Because most pulverized particles were close to 100 µm in diameter prior to devolatilization, the scale factors ranged only between 0.663 and 1.411.

The unresolved porosity of the microporous solid regions, θ_{mps}, was set to 25.6% for all particles. All transport and thermodynamic parameters and all kinetic parameters, including the sub-grid-scale surface area per unit volume of the microporous solid regions, S (3.79×10^7 m^2_C/m^3), were identical for every particle in the distribution. Although these parameters are not based on experimental data for this coal char, they are consistent between particles and allow for an evaluation of the impacts of the large pore morphology. The resolved pore volume, V_{voids}, and the microporous solid volume, V_{mps}, differed between the particles, as did the spatial distribution and morphology of the resolved pores and voids. The resolved porosity of the particles, θ_{void}, ranged from 11.9% to 60.3%.

The particles were individually placed at the center of a spherical domain with a diameter of 1000 µm. Far-field boundary conditions of 1373 K, and mole fractions of 12% O_2, 10% H_2O, 74% CO_2, and 4% CO are based on the pre-flame region of a 100 kWth pilot scale furnace [44]. No relative velocity was imposed, as the small particles are treated as entrained in the surrounding flow. However, the velocity at the boundary was free to adjust itself according to Stefan flow effects, which resulted in a net flux away from the particles.

Figure 2 shows a cross-section of part of the computational domain for one particle. In the resolved voids and pores (blue regions of Fig. 2), as well as in the gas-phase boundary layer surrounding the porous particle (green region of Fig. 2), standard gas-phase conservation equations for mass, momentum, species, and thermal energy were employed. In this way, the large heterogeneities (voids, pores) which are not amenable to upscaling were treated in a mathematically valid manner [41]. Because the microporous char (red regions of Fig. 2) contains sub-micron pores that are amenable to upscaling, effective-continuum conservation equations for mass, momentum, species, and thermal energy were employed in these regions to account for the presence of both gas and solid phases. A mass source term was included in the continuity equation in these regions to account for the net production of gas species from heterogeneous reaction. All heterogeneous reactions occur on the unresolved surface area, S, of the microporous solid regions, because the resolved interfacial area was two and half orders of magnitude smaller than the unresolved surface area of the microporous solid (compare SV_{mps} to the resolved interfacial area in Table S1).
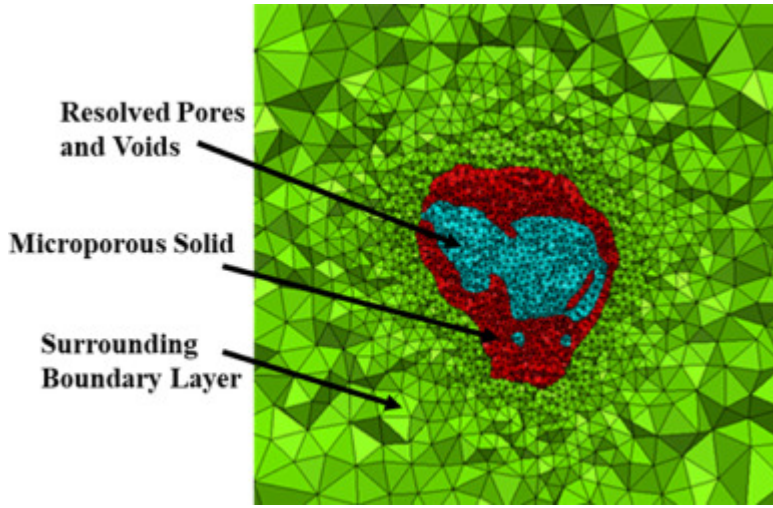
Fig. 2. Cross-section of a portion of the meshed computational domain for a char particle. Resolved pores/voids (blue), microporous solid (red) and part of the surrounding boundary layer (green). (For interpretation of the references to color in this figure caption, the reader is referred to the web version of this article.)

The submodels for transport and kinetic parameters and thermodynamic properties have been described previously [41] but are summarized briefly with a focus on the effective diffusion coefficient, which appears in the 1-D effectiveness factor models described in Section 2.4. In the microporous solid, both Knudsen and molecular diffusion were considered in formulating effective diffusion coefficients, D_{eff}, due to the small pore sizes in those regions. The Knudsen diffusion coefficient for species i is given by:

(2)

$$D_{i,Knud} = \frac{d_p}{3} \sqrt{\frac{8 R_u T}{\pi MW_i}}$$

where MW is molecular weight, T is the temperature, R_u is the gas constant and the mean pore diameter, d_p, is calculated using

(3)

$$d_p = \frac{4 \theta_{mps}}{S}$$

The effective diffusivity of the microporous solid is then calculated from $D_{i,Knud}$, the mixture-averaged molecular diffusion coefficient, $D_{i,m}$, the porosity, θ, and the tortuosity τ, which is taken to be unity

(4)

$$D_{i,eff} = \frac{1}{\left(\dfrac{1}{\frac{\theta_{mps}}{\tau} D_{i,Knud}} + \dfrac{1}{\frac{\theta_{mps}}{\tau} D_{i,m}} \right)}$$

In the surrounding boundary layer and in the resolved voids, standard, gas-phase mixture-averaged diffusion coefficients were used. The viscosity and thermal conductivities were determined using kinetic theory and standard mixing rules, and the ideal gas equation was used.

Heterogeneous oxidation and gasification reactions were considered, but gasification reactions were nearly three order of magnitudes slower than oxidation at the conditions simulated. Power law (n^{th} order) expressions were employed for gasification and a 1st order expression was used for oxidation. Arrhenius rate constants with pre-exponential factors and activation energies based on the review in [4] were used and are the same as used in [45] (Table S2 in the Supplementary Material). Homogenous reactions and radiation were not considered, due to the small particle size, because radiation is assumed to be dominated by particle-to-particle radiation among particles of similar temperature [23], and to focus on the interplay between transport, heterogeneous reaction and morphology

Each segmented particle was individually meshed with tetrahedra using Scan IP's "+FE Free" meshing algorithm. A finer mesh was used in the particles and near the interface between microporous solid and voids, while a coarser mesh was employed in the boundary layer (see Fig. 2). The mesh was exported to ANSYS Fluent for steady-state simulation. Being a low Mach number, variable density problem, the pressure-based solver was used for solving the governing equations, using the coupled algorithm. The power law scheme was used for most spatial finite volume discretizations, but the PRESTO! scheme was used to compute the pressure.

A mesh study was performed to ensure that the solution was converged with respect to the spatial discretization. Three meshes (consisting of approximately one million, two million and four million elements) were used to compute the steady state solution for a particle chosen at random. The oxygen mole fraction, a variable which varies drastically and irregularly throughout the computational domain (as will be seen in Section 3), was averaged over polar and azimuthal directions and plotted versus radius in Fig. 3. The relative error for the one- and two-million element meshes was 0.0173 and 0.0144, respectively. A mesh of approximately two million elements was deemed sufficient and used for each of the 50 particles. The computation time for each 3-D particle with a two million element mesh was approximately 140 h on a 28-core CPU.
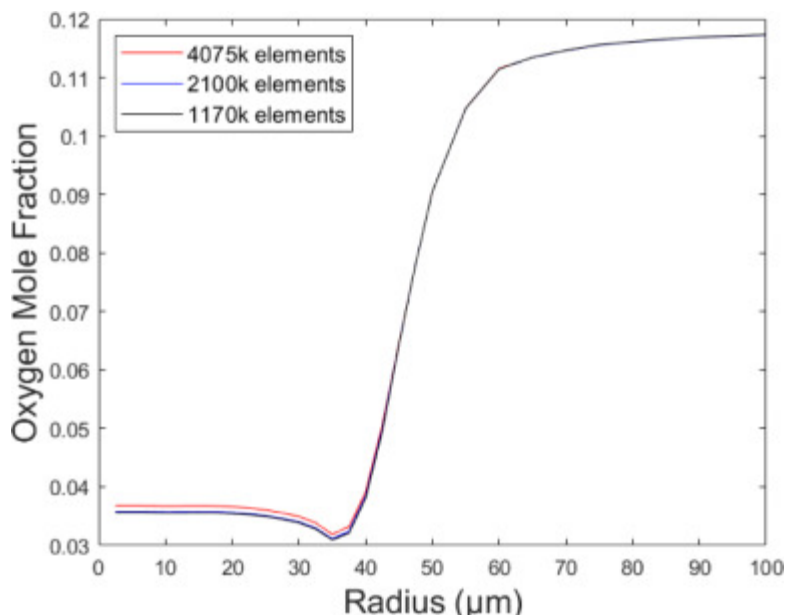

Fig 3. Comparison of directionally averaged oxygen mole fraction for different meshes.

2.4. Effectiveness factor calculations

The effectiveness factor, η, represents the ratio of the actual rate of reaction in a porous particle to the ideal rate of reaction in the absence of transport limitations. Using the results of the 3-D CFD simulations, the

effectiveness factor for oxidation for each real char particle was calculated according to its definition, using numerical integration over the microporous solid regions,

(5)

$$\eta_{3-D} = \frac{\int \int \int R_{actual} dV}{\int \int \int R_{ideal} dV}$$

The actual reaction rate, R_{actual}, which varies spatially, uses the calculated values for the oxygen mole fraction obtained from the 3-D simulation at each position. The ideal reaction rate, R_{ideal}, is calculated in the same way, except it uses a uniform reactant concentration throughout the particle equal to its boundary value, which would prevail in the absence of transport limitations. In the context of reactor-scale CFD codes, the actual reaction rate for a particle is determined by evaluating the ideal reaction rate using Eulerian-phase data for the cell containing the particle and multiplying by the effectiveness factor, η, which is evaluated using a 1-D model.

To assess the accuracy of 1-D effectiveness factor models amenable for use in reactor-scale codes, their predictions are compared to the "exact" effectiveness factors from the 3-D pore resolving CFD simulations. The formulation of the 1-D effectiveness factor models are presented for the case of a first order reaction, consistent with the rate expression for oxidation used in the pore-resolving simulation (Table S2), although effectiveness factors for nonlinear rate expressions are possible. To ensure a faithful comparison between the predictions of the 3-D pore resolving simulation and the 1-D effectiveness factor models for each of the 50 particles, the latter employed geometric and morphological parameters (interfacial area, void porosity, etc.) obtained from micro-CT image analysis of each particle. The predictions of the 3-D models are not used to tune the 1-D effectiveness factor models in any way.

2.4.1. Effectiveness factors for a uniform sphere and flat plate
Uniform sphere

The classical expression for the effectiveness factor of a uniformly porous, symmetrical sphere is given by

(6)

$$\eta = \frac{3}{\phi} \left(\frac{1}{\tanh(\phi)} - \frac{1}{\phi} \right)$$

where ϕ, the Thiele modulus, represents the ratio of the reaction rate to the diffusion rate within the porous particle. For a first order reaction, it is given by [46]

(7)

$$\phi = R \sqrt{\frac{S(1 - \theta_{void})k}{D_{eff}}}$$

where R is the particle radius, k is the intrinsic (per unit area) heterogeneous rate constant of the solid divided by its density (with resultant units of length per time) and S, θ_{void} and D_{eff} have been defined. For each particle, the radius, R can be calculated using the 3-D geometries obtained from micro-CT by averaging the distance from each node on the interface between the particle and the surrounding boundary layer to the particle's center. However, due to the scaling represented by Eq. (1), R was 50 μm for all particles in this study.

The uniform sphere model is unique among the 1-D models to be examined in that it does not account for the void porosity, θ_{void}, in calculating the length scale of the 1-D particle. Therefore, to ensure that the mass of carbon and total internal surface area per particle are consistent with the corresponding 3-D simulation, the

reactive surface area, S, of the uniform sphere model includes the factor $(1 - \theta_{void})$, which represents the volume fraction of microporous solid in each particle.

Due to the uniform sphere model's treatment of the large void porosity at the sub-grid-scale, there is some ambiguity as to whether the total porosity

(8)

$$\theta_{Total} = \theta_{void} + \theta_{mps}(1 - \theta_{void})$$

or the porosity of the microporous solid regions, θ_{mps}, should be used when calculating the Knudsen diffusivity, D_{Knud}. Consistent with the approach of Hodge et al. [14,47] who compared effectiveness factor models to experimental data, the average pore diameter, d_{pore}, and D_{Knud} were calculated using θ_{mps}, which is based on the nanometer-scale micro- and meso-pores through which Knudsen diffusion is dominant, while the molecular diffusion coefficient, D_m, is evaluated using θ_{Total}.

For each particle simulated, the porosity of the large pores and voids, θ_{void}, is obtained from the quotient of V_{mps} and $(V_{mps} + V_{voids})$, where the volume of each region was calculated using volume integration of the 3-D geometries obtained from micro-CT imaging (see tables S1 and S3 in the Supplementary Material for individual particle data).

Flat plate

Based on experimental evidence, it has been suggested that cenospherical and network char particles may be more accurately modeled as flat plates rather than uniform spheres [14]. The classical solution for the effectiveness factor of an infinite flat plate of thickness, L, is given by

(9)

$$\eta = \frac{\tanh\phi}{\phi}$$

where the Thiele modulus is given by

(10)

$$\phi = \frac{L}{2}\sqrt{\frac{Sk}{D_{eff}}}$$

Treating each particle as a symmetric hollow sphere, the cenosphere wall thickness, L, which corresponds to the plate thickness, was calculated using the particle radius, R, and the porosity of the resolved pores and voids, θ_{void}

(11)

$$L = R\left(1 - \theta_{void}^{\frac{1}{3}}\right)$$

It is seen in Eq. (11) that in the flat plate model (as well as in the other 1-D models to follow) the presence of large pores and voids is considered when formulating the geometry of the 1-D particle. In other words, the plate thickness, L, is based solely on the volume of microporous solid, V_{mps} and the large void porosity is not treated as sub-grid-scale. Thus, the surface area, S, in Eq. (10) need not include the factor $(1 - \theta_{void})$, and the effective diffusivity, D_{eff}, is unambiguously calculated using θ_{mps}.

2.4.2. Effectiveness factor for a hollow sphere

Buffham developed a lesser-known analytical solution for the effectiveness factor of a symmetric hollow sphere [48], which may be more appropriate than the flat plate model for cenospheres, especially those with thicker walls. The effectiveness factor for a hollow sphere is given by

(12)

$$\eta = \frac{3}{\phi\left(1 - \frac{R_{in}}{R_{out}}\right)}\left(\frac{\coth\left(\phi\left(1 - \frac{R_{in}}{R_{out}}\right)\right) + \phi\frac{R_{in}}{R_{out}}}{1 + \phi\frac{R_{in}}{R_{out}}\coth\left(\phi\left(1 - \frac{R_{in}}{R_{out}}\right)\right)} - \frac{1}{\phi}\right)$$

where R_{in} and R_{out} are the inner and outer radii, and the Thiele modulus ϕ is

(13)

$$\phi = R_{out}\sqrt{\frac{Sk}{D_{eff}}}$$

R_{out} is identical to R, as previously defined, while the inner radius was calculated using the geometry of a hollow sphere, with θ_{void} from volume integration of the 3-D particles

(14)

$$R_{in} = R_{out}\theta_{void}^{\frac{1}{3}}$$

The boundary conditions that were used to arrive at the analytical solution are a no flux condition at the center of the sphere and a fixed concentration at the external surface, which are identical to those used in deriving the effectiveness factor for a uniform sphere.

2.4.3. Effectiveness factors for complex 3-D structures

Another class of effectiveness factor models has been formulated to account for the complex three-dimensional structure of many catalyst particles in a one-dimensional framework [49], [50], [51], extending earlier approaches which use a particle's volume to surface area ratio as the characteristic length-scale [52], [53], [54]. The generalized cylinder (1D-GC) and variable diffusivity (1D-VD) models, as outlined in [49,50], require a detailed characterization of the particle's morphology, but have shown excellent accuracy in reproducing full 3-D calculations for catalyst applications (3% and 1% maximum error, respectively [49]). These models require assumptions of isotropic microporous regions, uniform reactivity in the microporous region, and uniform temperature and composition along the interface between the microporous solid and the surrounding fluid. This last assumption will be discussed in Section 3.

1D-CG models

The 1D-GC model requires the solution of a 1-D reaction-diffusion equation for the (dimensionless) reactant concentration, Y, along the (dimensionless) coordinate, z, with dimensionless reaction rate $r(Y)$ and variable cross-section with shape factor, σ [50]:

(15a)

$$z^{-\sigma}\frac{d}{dz}\left(z^{\sigma}\frac{dY}{dz}\right) = (1 + \sigma)^2\phi_{1D-GC}^2 r(Y)$$

with boundary conditions

(15b)

$$Y = 1 \text{ at } z = 1$$

(15c)

$$\frac{dY}{dz} = 0 \text{ at } z = 0$$

The Thiele modulus, ϕ_{1D-GC}, is given (for an irreversible reaction) by

(16)

$$\phi_{1D-GC} = l \sqrt{\frac{Sk}{D_{eff}}}$$

where the characteristic length l, represents the ratio of the particle volume to its interfacial area. In the present context, the characteristic length, l, corresponds to

(17)

$$l = \frac{V_{mps}}{S_{mps,interface}}$$

where $S_{mps,interface}$ is the interfacial area between microporous solid and resolved voids or external boundary layer (the interface between red and blue regions, as well as red and green regions, in Fig. 2). For each of the 50 particles, V_{mps} was calculated by volume integration and $S_{mps,interface}$ was calculated by surface integration over the interfaces in the 3-D structures obtained from micro-CT (see Table S3 in the Supplementary Material).

For the 1D-GCγ model (the variant of the model more appropriate at low Thiele modulus), the shape factor, σ, appearing in Eq. (15) requires the solution of Poisson's equation on the particle's surface [50]. The shape factor is given in terms of parameter γ

(18)

$$\sigma = \frac{3\gamma - 1}{1 - \gamma}$$

where

(19)

$$\gamma = \frac{\int \int \int G dV_{mps}}{V_{mps}}$$

and G is obtained from solving (dimensionless) Poisson's equation on the microporous solid domain

(20)

$$\nabla^{*2} G = -1 \text{ in } V_{mps}$$

subject to boundary condition

(21)

$$G = 0 \text{on} S_{mps,interface}$$

In this study, Poisson's equation for G was solved numerically using COMSOL for each real 3-D particle geometry obtained from micro-CT, followed by the calculation of γ and σ. In a reactor-scale CFD context, it is envisioned that these geometrical calculations would be performed for a representative distribution of particles as a preprocessing step and would not need to be performed within the effectiveness factor routine. The governing 1-D equation (Eq. (15)) was then solved numerically for Y, and the effectiveness factor calculated by numerical integration

(22)

$$\eta_{1D-GC} = (1 + \sigma) \int_0^1 r(Y) z^\sigma dz$$

For the 1D-GCΓ model [50] (the variant of the model more appropriate at high Thiele modulus), the shape factor, σ, is obtained from

(23)

$$\sigma = \frac{\Gamma}{1 - \Gamma}$$

where the geometric parameter, Γ, requires integration of the local principal radii of curvature over the particle's smooth interfacial area and its non-smooth edges, W, if present [55,56],

(24)

$$\Gamma = \frac{l}{S_{mps,interface}} \left(\int \int \left(\frac{1}{R_a} + \frac{1}{R_b} \right) dS_{mps,interface} + \int_W \mathcal{H} dW \right)$$

where R_a and R_b are the local principal radii of curvature on the particle's interfacial area and the non-smooth edge term, $\mathcal{H}$, is zero for naturally occurring char particles. For each real three-dimensional particle, R_a and R_b were calculated using COMSOL. The governing 1-D equation (Eq. (15)) was again solved numerically for Y, and the effectiveness factor calculated by numerical integration (Eq. (22)). The 1D-GC model parameters calculated for each particle are provided in Table S3 of the Supplementary Material.

1D-VD model

The 1D-VD model [50] employs a variable diffusivity along a single coordinate direction, x.

(25)

$$D_{eff}(x) = D_{eff} \Theta(x)$$

Where

(26)

$$\Theta(x) = \exp(C_1 x + C_2 x^\alpha)$$

The model requires three parameters [50] (C_1, C_2 and α) which are chosen such that the effectiveness factor matches the first three terms (including the zeroth order term) of the low modulus series expansion and the first two terms (including the zeroth order term) of the high modulus expansion [53]. In practice, the model's three

parameters require the solution of Poisson's equation for G on the particle's surface (Eq. (20)) to obtain γ from Eq. (19) and β from

(27)

$$\beta = \frac{\iiint G^2 dV_{mps}}{V_{mps}}$$

as well as the integration of R_a and R_b over the particle's smooth surface and non-smooth "edges" angles (to obtain Γ from Eq. (24)). Parameter C1 is obtained from

(28)

$$C_1 = -2\Gamma$$

while C_2 and α are obtained from simultaneously solving nonlinear equations [50]

(29)

$$\gamma = \int_0^1 \frac{(1-x)^2}{\Theta(x)} dx$$

(30)

$$\beta = \int_0^1 F^2(x) dx$$

(31)

$$F(x) = \int_0^x \frac{(1-x_0)}{\Theta(x_0)} dx$$

Again, in the context of a reactor-scale CFD code, these calculations would be performed outside of the effectiveness factor routine. The effectiveness factor requires the numerical solution of a 1-D boundary value problem to obtain the concentration profile

(32a)

$$\frac{d}{dx}\left(\Theta(x)\frac{dY}{dx}\right) = \phi_{1D-VD}^2 r(Y)$$

(32b)

$$Y = 1 \,\mathrm{at}\, x = 0$$

(32c)

$$\frac{dY}{dx} = 0 \,\mathrm{at}\, x = 1$$

where the Thiele modulus is evaluated from Eq. (16). The dimensionless Y was then used in integrating the dimensionless reaction rate to yield the effectiveness factor [50]

(33)

$$\eta_{1D-VD} = \int_0^1 r(Y)dx$$

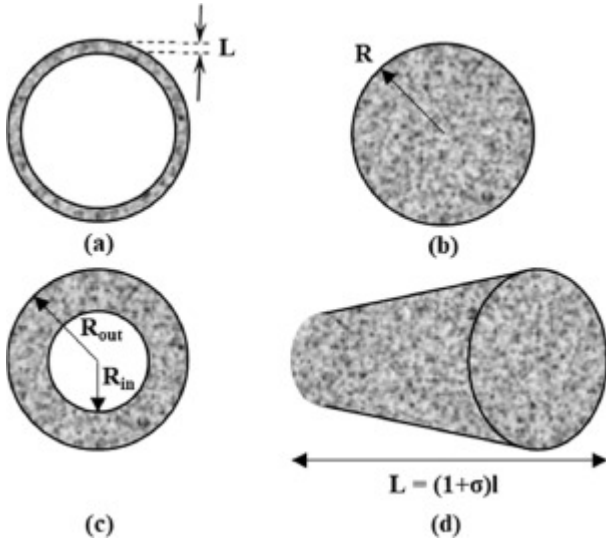A visual representation of the 1D effectiveness factor models is shown in Fig. 4.

Fig. 4. Visual representation of 1D effectiveness factor models with relevant length scales, for (a) flat plate, (b) uniform sphere, (c) hollow sphere, and (d) 1D-GC models.

3. Results and discussion

All parameters (reaction rates, diffusion coefficients, sub-grid scale surface area, etc.) were identical in the 3-D and 1-D models for each particle. Temperature-dependent parameters in the 1-D model used the volume averaged temperature for each particle calculated from the corresponding 3-D model. Nonetheless, 1-D effectiveness factor models solve a single, simplified reaction-diffusion equation, while the 3-D CFD simulation solves conservation equations for mass, momentum, n-1 species and thermal energy . Therefore, to ensure that the 3-D simulation and the 1-D effectiveness factor models are comparable and that differences are primarily due to the impacts of realistic particle geometries, a 3-D pore resolving simulation was run for a uniformly porous sphere at steady state and compared to the 1-D analytical solution [46]. The effectiveness factor calculated from the CFD simulation was 0.475, which was in close agreement with the value of 0.486 calculated using the classical effectiveness factor model, indicating that any differences observed for the real char particles are primarily due to their geometrical complexities. The small difference is attributed to the additional physics captured in the CFD simulation, such as the impacts of Stefan flow and the presence of product species.

Studies have established, at least for simpler geometries, that the instantaneous distribution of species in reacting char particles is approximately quasi-steady at any time [57,58]. In other words, a transient simulation for a reacting pulverized char particle would be closely represented by a series of steady state simulations at different levels of char conversion. This implies that steady-state simulations provide an accurate representation of the transport-reaction coupling for a *given* morphology. However, a comparison between steady-state and transient solutions was performed to ensure that the former provides an adequate representation of the latter for the complex char particles and conditions simulated in this study.

Radial distributions of oxygen mole fraction averaged over polar and azimuthal angles are compared for transient [41] and steady-state simulations in Fig. 5, for three particles. The predictions are compared at (an early time of) 25 ms to minimize the degree of structural evolution that occurred in the transient simulation. The reason that an even earlier time was not used for comparison is because fast transients exist at the beginning of the unsteady simulation as the species profiles adjust to the imposition of the boundary conditions. All three particles yielded similar results for both transient and steady simulations, with average relative differences of 6.93%, 4.63%, 4.46%. Some, or perhaps most, of this difference can be attributed to the carbon conversion that occurred in the first 25 ms of the transient simulation. It is concluded that steady state simulations are reasonable representations of the interplay of reaction and diffusion for a given morphology and therefore sufficient for the purposes of this study.
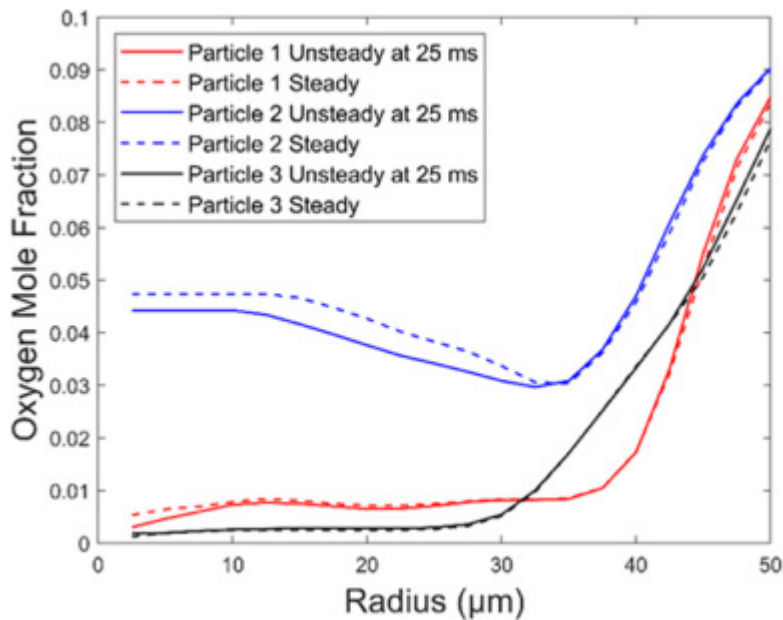

Fig. 5. Comparison of directionally averaged oxygen mole fraction within three different particles for steady and transient simulations.

The combustion of 50 char particles imaged with high-resolution micro-CT was then simulated using the pore-resolving CFD model, with approximately two million elements per particle. Figure 6 shows 3-D morphologies of six representative char particles ranging from highly cenospherical to more complex pore structures (Fig. 6(a)), as well as the oxygen mole fraction distributions (Fig. 6(b)) and temperature distributions (Fig. 6(c)) for planes passing through the centers of the same particles. It is noted that the oxygen mole fraction and temperature are shown for both the resolved pores and the microporous char regions.
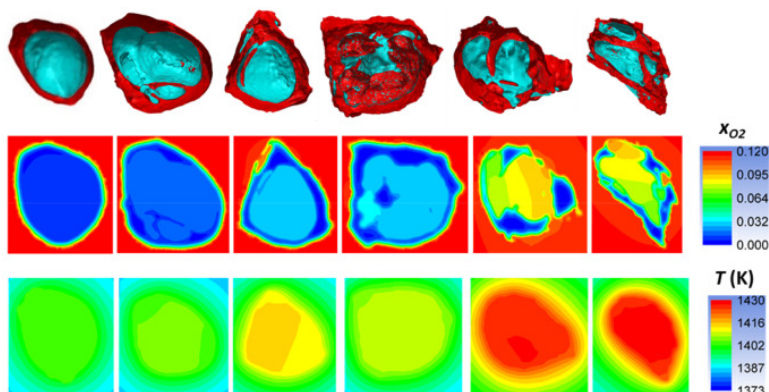
Fig. 6. (a) Three dimensional geometries of six particles, showing microporous char (red) and resolved pores and voids (blue), together with, (b) oxygen mole fraction distributions, and (c) temperature distributions, for two dimensional sections of the same particles. (For interpretation of the references to color in this figure legend, the reader is referred to the web version of this article.)

It is observed in Fig. 6(b) that the oxygen mole fraction distribution is highly dependent on the structure of the large voids and pores and is elevated in those regions. For all char particles, the minimum oxygen mole fraction is located within the microporous char and not at the particle center. This indicates that for most particles, small holes exist that allow for enhanced transport between the particles' interior voids and the external surface. Even for the most cenospherical particle (the leftmost particle in Fig. 6), the minimum oxygen mole fraction occurs in the thickest region of microporous solid, although the concentration in the void is only slightly higher than its minimum value due to the lack of holes on the surface of this particle (this was verified in three dimensions). For the more complex network-type char structures, the oxygen mole fraction is highly asymmetric and does not vary monotonically between the particle surface and its center.

In contrast to the highly non-uniform oxygen mole fraction, the temperature distribution is nearly spatially uniform and does not exhibit marked differences between the resolved pores and the microporous char, as shown in Fig. 6(c). The observed temperature gradients reside primarily around the outer edge of the particles. This is not unexpected, due to the small size of the pulverized char particles, their relatively high thermal conductivity and the quiescent atmosphere associated with particles assumed to be entrained in the surrounding flow. This gives rise to a Biot number much smaller than unity and nearly uniform internal temperatures. It is noted that this conclusion may not hold in conditions closer to zone III (diffusion-limited) combustion in which the temperature rise would be higher. The volume averaged particle temperature for the hottest burning particle was 1430 K, while for the coolest particle it was 1403 K.

The effectiveness factors for the real char particles were obtained from numerical integration of the 3-D data using Eq. (5). These "exact" effectiveness factors are compared to one another, and to the effectiveness factors for uniform spheres, flat plates and hollow spheres, which can be calculated analytically using Eqs. (6), (9) and (12), in Fig. 6. Many reactor-scale studies use effectiveness factors for uniform spheres for the tracked particles (e.g., [59,60]). Hodge et al. proposed using flat plate effectiveness factors for cenospherical and network particles [14], while Ma and Mitchell have proposed treating particles with large voids using correlations involving the effectiveness factor of a uniform sphere and the void porosity [13].

For comparison between the pore-resolving model and the effectiveness factor models, the particles are arranged on the abscissa in increasing order of the external void fraction (EVF), an indicator which increases as particles transition from cenospheres with isolated voids to more complex and connected pore structures. The EVF is defined as

(34)

$$\text{EVF} = \frac{S_{ext,void}}{S_{ext,total}}$$

where $S_{ext,total}$ is the total interfacial area between the particle the surrounding boundary layer (the green/red and green/blue interface areas in Fig. 2), and $S_{ext,void}$ represents the interface area between the voids and the surrounding boundary layer (the green/blue interface in Fig. 2). This ratio decreases as the particles becomes more cenospherical, with a single, isolated central void, and increases for particles with more numerous and complex pores that penetrate the particle surface. In other words, the order of particles along the abscissa

places the (mostly thick-walled) cenospheres on the left and the more connected, complex pore structures on the right.

It is first observed in Fig. 7 that the true, 3-D effectiveness factors (and thus the reaction rates, via Eq. (5)) exhibit a two- to three-fold particle-to-particle variation, despite all particles having the same effective diameter and reacting under the same conditions. This suggests that reactor-scale CFD codes, which often incorporate a distribution of particle sizes, should also consider incorporating a distribution of porosity and/or morphology. It is noted, however, that a size distribution of particles of uniform porosity accounts for mass variations, which contributes to the variability seen in Fig. 7.
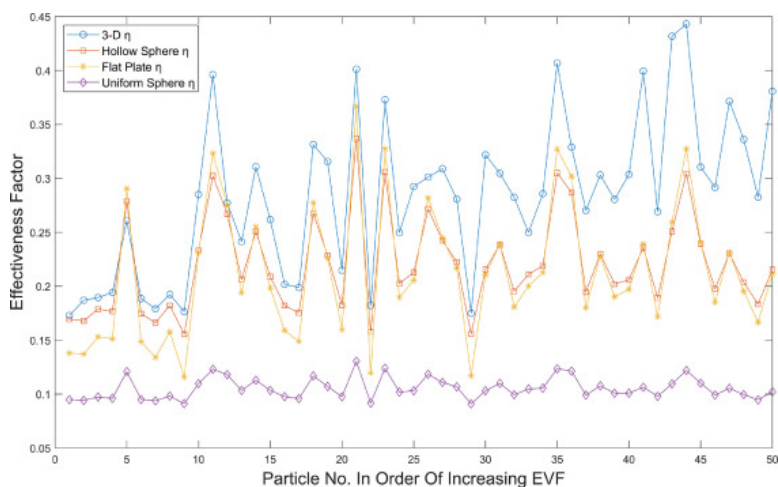

Fig. 7. Comparison of effectiveness factors predicted by classical models with effectiveness factor obtained by volume integration of the 3-D, pore-resolving simulation data.

The uniform sphere effectiveness factor model treats all porosity as sub-grid scale and overestimates the characteristic diffusion length. In this model, large pores do not act as reactant reservoirs or channels and gas only penetrates the particle by diffusing through uniformly porous solid. As it has been experimentally demonstrated that the uniform sphere method is not suitable for realistic particles with multiple large pores [14], it is not surprising to see, in Fig. 7, that the uniform sphere model using the same diffusion model (Section 2.4.1) predicts the lowest effectiveness factor and is the least accurate compared to the 3-D solution. It is noted, that if d_{pore} is calculated using the total porosity, the agreement with the 3-D solution would improve, as the overestimation of the D_{Knud} would offset the error in the characteristic length scale. Another option to reduce the error of the uniform sphere model would be to use a uniform sphere whose radius is smaller and based only on V_{mps}.

The analytical solutions for hollow spheres and flat plates provide reasonable approximations to the exact effectiveness factors for censpherical particles, as seen in Fig. 7. These two models account for the presence of large voids and incorporate a shorter length-scale for diffusion through the microporous solid (see Eqs. (11) and (14)). While the two models yield similar predictions, the hollow sphere model is more accurate for cenospherical particles, which is the particle type for which these models provide a reasonable prediction (8.4% relative error vs. 21.7% relative error for particles 1–10). This is because a flat plate is a less realistic geometry than a hollow sphere, especially for thicker-walled cenospheres. For all 50 particles, the hollow sphere model yields an average relative error of 20.7%, compared with 25.3% for the flat plate model. For the more complex structures on the right of the abscissa, neither the flat plate nor the hollow sphere models are accurate, with average errors of 31.3% and 30.0% for particles 30 to 50. Effectiveness factors for each particle are provided in Table S4 of the Supplementary Material.

Despite its accuracy for censpheres, the hollow sphere model predicts lower effectiveness factors than the true 3-D effectiveness factors for all particle types. This is likely because the central void in the hollow sphere model is inaccessible and oxygen must first penetrate through the microporous solid region. For most real char particles, however, large pores that extend to the particle surface allow oxygen to channel throughout the particle, as seen in Fig. 6(b), particularly for the network-type particles. Furthermore, it has been shown previously in a study of a single resolved char particle that large macropores and voids also increase the penetration of reactant into the microporous solid regions to a larger extent than predictions of uniform porosity effective continuum models [41]. This is because the large pore networks present in real char particles act as reservoirs for reactant and decrease the effective length-scale for diffusion within the adjacent microporous solid, which increases the effectiveness factor.

This observation has been corroborated in Fig. 8, in which the oxygen mole fraction calculated by the pore-resolving simulations, x_{O2}, within microporous solid regions is averaged over polar and azimuthal angles at every radial position, using

(35)

$$x_{O2,mps} = \frac{\int_0^{2\pi} \int_0^{\pi} \delta x_{O2}(r,\theta,\varphi) r^2 \sin(\theta) d\theta d\varphi}{\int_0^{2\pi} \int_0^{\pi} \delta r^2 \sin(\theta) d\theta d\varphi}$$

where δ is unity for microporous solid regions and zero elsewhere. Microporous solid oxygen mole fraction distributions are shown for 15 representative particles in Fig. 8: five cenospheres ("Group 1"), five transitional particle ("Group 2"), and five particles with network structures ("Group 3"). The plot lines are interrupted when there is no microporous solid at a particular radial position.
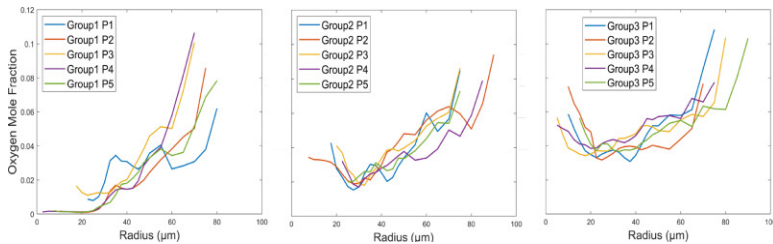

Fig. 8. Oxygen mole fraction in the microporous solid as a function of radius (averaged over polar and azimuthal angles) for 5 particles (P1-P5) from (a) cenospherical, (b) transitional and (c) network particle groups calculated from the pore-resolving simulation.

The oxygen mole fraction on the external surface is similar across all groups, and all three groups exhibit a sharp decrease in the oxygen mole fraction between the external surface and a radius of ~40 μm. This drop is likely due to those points being comprised of protrusions where the average oxygen mole fraction is high, and the reaction rate is correspondingly fast.

More pronounced differences are observed in Fig. 8 near the center of the particles. For Group 1, the oxygen mole fraction keeps decreasing in microporous solid regions toward the particle center until it approaches or reaches zero. Conversely, for Groups 2 and 3, the oxygen mole fraction within the microporous solid *increases* toward the particle center. In fact, for some particles in Group 3, the oxygen mole fraction in microporous regions near the particle center approaches its surface value. The large pores connected to the external surface facilitate the transport of oxygen throughout the particle and the characteristic length-scale for diffusion within the solid is much smaller than the particle radius. This leads to higher oxygen concentration in

the microporous solid in the complex particles compared to the particles that have isolated central voids, as seen in Fig. 8.

Effectiveness factors calculated using the more complex 1D-GCγ, 1D-GCΓ and 1D-VD models are shown in Fig. 9, in which effectiveness factors from the 3-D, pore-resolving model and the hollow sphere effectiveness factor model are also shown. Several geometric parameters are incorporated in the 1D-GCγ, 1D-GCΓ and 1D-VD models, as described in Section 2.4.3, which led to very high accuracy in catalyst applications [49,50]. It is observed in Fig. 9 that the 1D-GCγ, 1D-GCΓ and 1D-VD models produce similar effectiveness factor predictions. Compared to the 1D-GCγ model, which predicts the lowest effectiveness factors, the 1D-VD and 1D-GCΓ models yield an average of 4.8% and 8.4% higher values, respectively. All three models predict higher effectiveness factors than the 3-D pore-resolving simulations, with an over-prediction of 55.6% for the most cenospherical particles (particles 1 to 10) and 16.8% for the more connected, network-type particles (particles 40 to 50). Effectiveness factors calculated for each particle are provided in Table S4 of the Supplementary Material.
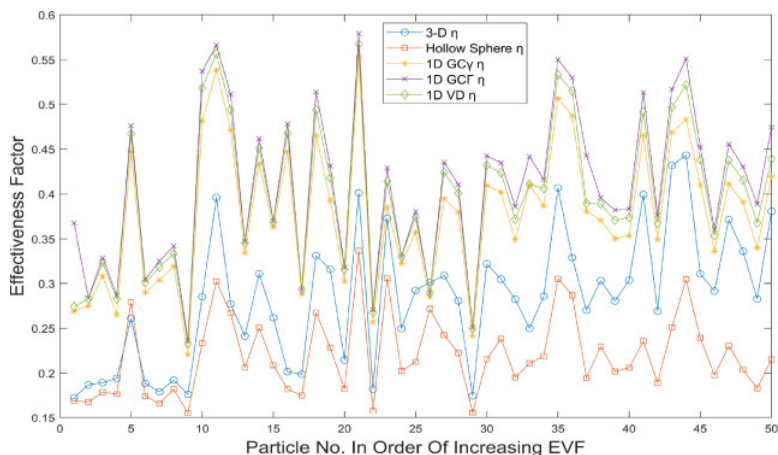

Fig. 9. Comparison of effectiveness factors predicted by 1D-GC and 1D-VD models with the hollow sphere model and with effectiveness factor obtained by volume integration of the 3-D, pore-resolving simulation data.

The 1D-GCγ, 1D-GCΓ and 1D-VD models incorporate several assumptions, noted in Section 2.4.3, which includes the restrictive assumption, for high temperature combustion and gasification applications, of uniform reactant concentration along the interface between the microporous solid and external surface/voids (the red/blue and red/green interfaces in Fig. 2). In reality, oxygen concentration gradients exist within the void space, which reduces the interfacial oxygen mole fraction at locations toward the particle centers, as seen in Fig. (6b). This reduction in interfacial oxygen mole fraction results in true (3-D) effectiveness factors which are lower than the predictions of the 1D-GC and 1D-VD models.

Particles with macropores extending to the surface (particles toward the right of the abscissa in Fig. 9) have a more uniform oxygen mole fraction on the microporous solid/void interface than cenospheres, whose inner wall is largely disconnected from the surface. The connected voids and pore networks facilitate the transport of oxygen to the entire pore network, whereas oxygen reaches the inner wall of the most cenospherical particles predominantly by transport through the microporous solid. This leads to better accuracy (smaller overprediction of effectiveness factors) for the 1D-GC and 1D-VD for the more complex, connected void structures than the more cenospherical structures, as seen in Fig. 9.

The relatively higher oxygen mole fraction throughout the void space of the more complex particles is verified in Fig. 10, in which the oxygen mole fraction within the resolved pores is averaged over polar and azimuthal angles at every radial position for the same 15 particles shown in Fig. 8. To obtain the data in Fig. 10, Eq. (35) is again used, but in this case δ is unity for the resolved pores and zero in other regions. For the cenospherical

particles (Group 1) the oxygen mole fraction is nearly uniform in the void space and significantly lower than its surface value, due to the near isolation of the central void from the external surface. For the transitional (Group 2) and network-type (Group 3 – highest EVF) particles, the oxygen mole fraction is higher in the large pores and voids due to their connectedness to the external surface.
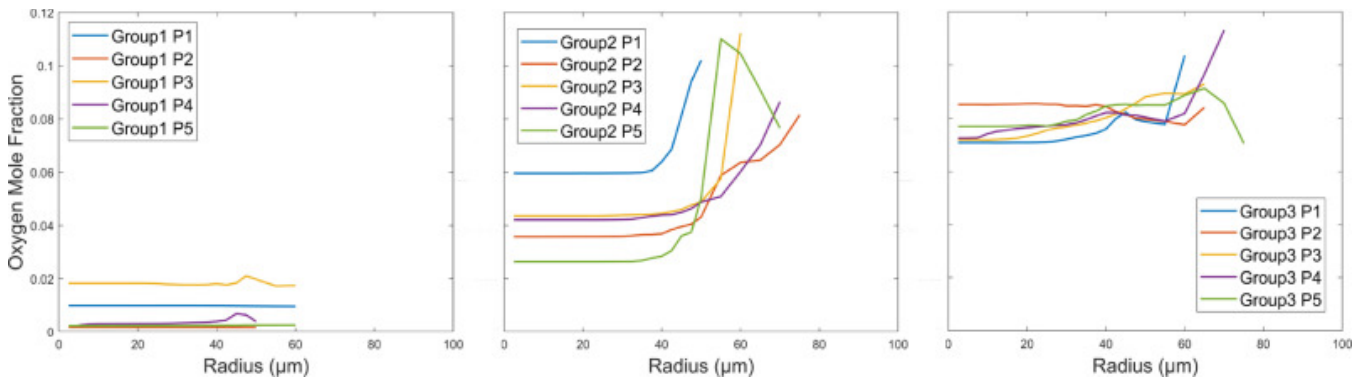

Fig. 10. Oxygen mole fraction in the resolved pores and voids as a function of radius (after averaging over polar and azimuthal angles) for (a) cenosphericalCenospherical, (b), transitional and (c), network particles calculated from the pore-resolving simulation.

4. Conclusions

High-resolution micro-CT imaging (voxel size of 1.632 µm) was performed for pulverized coal char particles (105 µm nominal diameter) to obtain the internal and external geometries in 3-D. The first pore-resolving, zone II combustion simulations for real char particles were then carried out for 50 particles. The pore-resolving simulations respect the separation of length-scales required for effective-continuum treatments of porous media, by applying equations based on first principles in the resolved pores and the surrounding boundary layer, and only using effective-continuum conservation equations in the microporous solid regions where the pore size is much smaller than the size of the particles.

The reactant (oxygen) mole fraction distribution in real char particles is highly dependent on the morphology of large pores and voids, is non-monotonic with distance from the particle's surface and attains local minima within thick microporous char regions irrespective of the distance from the external surface. The prevalence of complex interconnected large pore networks that extend to the external surface enhances oxygen transport throughout the particle, even within microporous solid regions near the particles' centers. Conversely, temperatures were nearly spatially uniform throughout the particles, irrespective of the void morphology, for the zone II conditions examined in this study.

Because reactor-scale CFD simulations require one-dimensional models for the thousands of tracked char particles, predictions of effectiveness factor models have been compared with the effectiveness factors calculated from the 3-D pore-resolving simulations. Effectiveness factors predicted from the classical uniform sphere model, a flat plate model, a hollow sphere model, and the 1D-GC and 1D-VD models were assessed. The commonly used uniform sphere model treats all pores as sub-grid-scale and results in effectiveness factors which are too low for all particle types. The hollow sphere model produces good agreement (better than the flat plate model) with the pore-resolving simulation for char particles which are cenospherical but is inaccurate for particles with more complex pore structures. Although the 1D-GC and 1D-VD models account for the three-dimensional morphology of real particles, they overpredict the effectiveness factors for all particle types due to their assumption of uniform reactant concentration along the entire solid/void interface. This assumption is particularly inaccurate for cenospheres with minimal connection between the central void and external surface.

Zone II combustion of cenospherical char can be adequately modeled in a one-dimensional context using the hollow sphere effectiveness factor approach. More complex network-type char particles require either a new effectiveness factor approach, a modification of the 1D-GC or 1D-VD models to account for non-uniform interface concentration, or perhaps a modification of bimodal ("macro-micropore") effectiveness factor models [61] to account for "macropores" that cannot be treated at the sub-grid-scale. Reactor-scale CFD codes, which often employ a distribution of particle sizes, should also include a distribution of morphologies and a corresponding distribution of effectiveness factor models, given the variation of reaction rates between particles of the same size reacting under the same conditions and the demonstrated impacts of morphology on 1-D effectiveness factor predictions.

Declaration of Competing Interest

The authors declare that they have no known competing financial interests or personal relationships that could have appeared to influence the work reported in this paper.

Acknowledgments

References

[1] P.A. Bejarano, Y.A. Levendis. **Combustion of coal chars in oxygen-enriched atmospheres.** Combust. Sci. Technol., 179 (2007), pp. 1569-1587

[2] P.A. Bejarano, Y.A. Levendis. **Single-coal-particle combustion in O_2/N_2 and O_2/CO_2 environments.** Combust. Flame, 153 (2008), pp. 270-287

[3] J. Riaza, R. Khatami, Y.A. Levendis, L. Álvarez, M.V. Gil, C. Pevida, F. Rubiera, J.J. Pis. **Single particle ignition and combustion of anthracite, semi-anthracite and bituminous coals in air and simulated oxy-fuel conditions.** Combust. Flame, 161 (2014), pp. 1096-1108

[4] E.S. Hecht, C.R. Shaddix, A. Molina, B.S. Haynes. **Effect of CO_2 gasification reaction on oxy-combustion of pulverized coal char.** Proc. Combust. Inst., 33 (2011), pp. 1699-1706

[5] L. Álvarez, C. Yin, J. Riaza, C. Pevida, J.J. Pis, F. Rubiera. **Biomass co-firing under oxy-fuel conditions: a computational fluid dynamics modelling study and experimental validation.** Fuel Process. Technol., 120 (2014), pp. 22-33

[6] S.L. Singer, A.F. Ghoniem. **Comprehensive gasification modeling of char particles with multi-modal pore structures.** Combust. Flame, 160 (2013), pp. 120-137

[7] S. Schulze, A. Richter, M. Vascellari, A. Gupta, B. Meyer, P.A. Nikrityuk. **Novel intrinsic-based submodel for char particle gasification in entrained-flow gasifiers: model development, validation and illustration.** Appl. Energy., 164 (2016), pp. 805-814

[8] U. Kleinhans, S. Halama, H. Spliethoff. **The role of gasification reactions during pulverized solid fuel combustion: a detailed char combustion model based on measurements of char structure and kinetics for coal and pre-treated biomass.** Combust. Flame, 184 (2017), pp. 117-135

[9] S.R. Gubba, L. Ma, M. Pourkashanian, A. Williams. **Influence of particle shape and internal thermal gradients of biomass particles on pulverised coal/biomass co-fired flames.** Fuel Process. Technol., 92 (2011), pp. 2185-2195

[10] M. Kumar, A.F. Ghoniem. **Multiphysics simulations of entrained flow gasification. Part I: validating the nonreacting flow solver and the particle turbulent dispersion model.** Energy Fuels, 26 (2012), pp. 451-463

[11] M. Vascellari, R. Arora, C. Hasse. **Simulation of entrained flow gasification with advanced coal conversion submodels. Part 2: char conversion.** Fuel, 118 (2014), pp. 369-384

[12] U. Kleinhans, S. Halama, H. Spliethoff. **Char particle burning behavior: experimental investigation of char structure evolution during pulverized fuel conversion.** Fuel Process. Technol., 171 (2018), pp. 361-373

[13] L. Ma, R. Mitchell. **Modeling char oxidation behavior under Zone II burning conditions at elevated pressures.** Combust. Flame, 156 (2009), pp. 37-50

[14] E.M. Hodge, D.G. Roberts, D.J. Harris, J.F. Stubington. **The significance of char morphology to the analysis of high-temperature char–CO_2 reaction rates.** Energy Fuels, 24 (2010), pp. 100-107

[15] S. Whitaker. **Diffusion and dispersion in porous media.** AIChE J., 13 (1967), pp. 420-427

[16] J. Auriault. **Upscaling heterogeneous media by asymptotic expansions.** J. Eng. Mech., 128 (2002), pp. 817-822

[17] R. Sahu, R.C. Flagan, G.R. Gavalas. **Discrete simulation of cenospheric coal-char combustion.** Combust. Flame, 77 (1989), pp. 337-346

[18] S. Whitaker. **The Method of Volume Averaging.** (1st Edition), Springer, Netherlands, Boston (1999)

[19] M. Sahimi, G.R. Gavalas, T.T. Tsotsis. **Statistical and continuum models of fluid-solid reactions in porous media.** Chem. Eng. Sci., 45 (1990), pp. 1443-1502

[20] A.M. Beckmann, J. Bibrzycki, M. Mancini, A. Szlek, R. Weber. **Mathematical modeling of reactants' transport and chemistry during oxidation of a millimeter-sized coal-char particle in a hot air stream.** Combust. Flame, 180 (2017), pp. 2-9

[21] C.B. Nguyen, J. Scherer, Q. Guo, S. Kriebitzsch, A. Richter. **The shape development of spherical and non-spherical char particles in the flame zone of an entrained-flow gasifier – A numerical study.** Int. J. Heat Mass Transf., 149 (2020), Article 119220

[22] C.B. Nguyen, J. Scherer, M. Hartwich, A. Richter. **The morphology evolution of char particles during conversion processes.** Combust. Flame, 226 (2021), pp. 117-128

[23] Y. Cai, K. Zygourakis. **A multiscale transient model for combustion of highly porous chars.** Ind. Eng. Chem. Res., 42 (2003), pp. 2746-2755

[24] F. Boso, I. Battiato. **Homogenizability conditions for multicomponent reactive transport processes.** Adv. Water Resour., 62 (2013), pp. 254-265

[25] E.M. Ryan, A.M. Tartakovsky, C. Amon. **Pore-scale modeling of competitive adsorption in porous media.** J. Contam. Hydrol., 120-121 (2011), pp. 56-78 120–121

[26] M. Sahraoui, M. Kaviany. **Direct simulation vs volume-averaged treatment of adiabatic, premixed flame in a porous medium.** Int. J. Heat Mass Transf., 37 (1994), pp. 2817-2834

[27] R. Jovanović, E. Marek, S. Maletić, D. Cvetinović, Z. Marković. **Lattice Monte Carlo simulation of single coal char particle combustion under oxy–fuel conditions.** Fuel, 151 (2015), pp. 172-181

[28] H. Xin, C. Wang, E. Louw, D. Wang, J.P. Mathews. **Atomistic simulation of coal char isothermal oxy-fuel combustion: char reactivity and behavior.** Fuel, 182 (2016), pp. 935-943

[29]
P.N. Ciesielski, M.F. Crowley, M.R. Nimlos, A.W. Sanders, G.M. Wiggins, D. Robichaud, B.S. Donohoe, T.D. Foust. **Biomass particle models with realistic morphology and resolved microstructure for simulations of intraparticle transport phenomena**. Energy Fuels, 29 (2015), pp. 242-254

[30] M.B. Pecha, M. Garcia-Perez, T.D. Foust, P.N. Ciesielski. **Estimation of heat transfer coefficients for biomass particles by direct numerical simulation using microstructured particle models in the laminar regime.** ACS Sustain. Chem. Eng., 5 (2017), pp. 1046-1053

[31] A. Richter, P.A. Nikrityuk, B. Meyer. **Three-dimensional calculation of a chemically reacting porous particle moving in a hot O_2/CO_2 atmosphere.** Int. J. Heat Mass Transf., 83 (2015), pp. 244-258

[32] Z. Xue, Q. Guo, Y. Gong, J. Xu, G. Yu. **Numerical study of a reacting single coal char particle with different pore structures moving in a hot O_2/CO_2 atmosphere.** Fuel, 206 (2017), pp. 381-389

[33] A.G. Dixon, M.E. Taskin, M. Nijemeisland, E.H. Stitt. **CFD method to couple three-dimensional transport and reaction inside catalyst particles to the fixed bed flow field.** Ind. Eng. Chem. Res., 49 (2010), pp. 9012-9025

[34] M.E. Taskin, A. Troupel, A.G. Dixon, M. Nijemeisland, E.H. Stitt. **Strongly endothermic reactions.** Ind. Eng. Chem Res., 49 (2010), pp. 9026-9037

[35] M. Behnam, A.G. Dixon, M. Nijemeisland, E.H. Stitt. **Catalyst deactivation in 3D CFD resolved particle simulations of propane dehydrogenation.** Ind. Eng. Chem. Res., 49 (2010), pp. 10641-10650

[36] A.G. Dixon, J. Boudreau, A. Rocheleau, A. Troupel, M.E. Taskin, M. Nijemeisland, E.H. Stitt. **Flow, transport, and reaction interactions in shaped cylindrical particles for steam methane reforming.** Ind. Eng. Chem. Res., 51 (2012), pp. 15839-15854

[37] J.P. Mathews, Q.P. Campbell, H. Xu, P. Halleck. **A review of the application of X-ray computed tomography to the study of coal.** Fuel, 209 (2017), pp. 10-24

[38] E. Boigné, N.R. Bennett, A. Wang, K. Mohri, M. Ihme. **Simultaneous in-situ measurements of gas temperature and pyrolysis of biomass smoldering via X-ray computed tomography.** Proc. Combust. Inst., 38 (2020), pp. 1-9

[39] H. Watanabe. **X-ray computed tomography visualization of the woody char intraparticle pore structure and its role on anisotropic evolution during char gasification.** Energy Fuels, 32 (2018), pp. 4248-4254

[40] X. Ni, J. Miao, R. Lv, X. Lin. **Quantitative 3D spatial characterization and flow simulation of coal macropores based on μCT technology.** Fuel, 200 (2017), pp. 199-207

[41] G. Fong, S. Jorgensen, S.L. Singer. **Pore-resolving simulation of char particle gasification using micro-CT.** Fuel, 224 (2018), pp. 752-763

[42] S. Jorgensen, S. Singer. **Micro-CT-based approaches for quantifying the morphology of pulverized char particles.** Energy Fuels, 33 (2019), pp. 4826-4834

[43] D. Alvarez, E. Lester. **Atlas of char occurrences.** International Conference on Coal Petroleum, Combustion Working Group Commission III (2001)

[44] S. Hjärtstam, K. Andersson, F. Johnsson, B. Leckner. **Combustion characteristics of lignite-fired oxy-fuel flames.** Fuel, 88 (2009), pp. 2216-2224

[45] S. Singer, L. Chen, A.F. Ghoniem. **The influence of gasification reactions on char consumption under oxy-combustion conditions: effects of particle trajectory and conversion.** Proc. Combust. Inst., 34 (2013), pp. 3471-3478

[46] E.W. Thiele. **Relation between catalytic activity and size of particle.** Ind. Eng. Chem., 31 (1939), pp. 916-920

[47] E.M. Hodge. **The Coal char-CO_2 Reaction At High Temperature and High Pressure.** University of New South Wales (2009)

[48] B.A. Buffham. **Design relations for hollow catalyst pellets.** Trans. Inst. Chem. Eng. A., 78 (2000), pp. 269-282

[49] C. Mocciaro, J. Mariani, O.M. Martínez, G.F. Barreto. **A Three-parameter one-dimensional model to predict the effectiveness factor for an arbitrary pellet shape.** Ind. Eng. Chem. Res., 50 (2011), pp. 2746-2754

[50] N.J. Mariani, M.J. Taulamet, S.D. Keegan, O.M. Martínez, G.F. Barreto. **Prediction of effectiveness factor using one-dimensional approximations for complex pellet shapes and abnormal kinetics expressions.** Ind. Eng. Chem. Res., 52 (2013), pp. 15321-15329

[51] A. Burghardt, A. Kubaczka. **Generalization of the effectiveness factor for any shape of a catalyst pellet.** Chem. Eng. Process. Process Intensif., 35 (1996), pp. 65-74

[52] R. Aris. **On shape factors for irregular particles-I: the Steady state problem. Diffusion and reaction.** Chem. Eng. Sci., 6 (1957), pp. 262-268

[53] R. Aris. **A normalization for the Thiele modulus.** Ind. Eng. Chem. Fundam., 4 (1965), pp. 227-229

[54] R. Datta, S. Leung. **Shape generalized isothermal effectiveness factor for first-order kinetics.** Chem. Eng. Commun., 39 (1985), pp. 155-173

[55] S.D. Keegan, N.J. Mariani, O.M. Martínez, G.F. Barreto. **Behaviour of smooth catalysts at high reaction rates.** Chem. Eng. J., 110 (2005), pp. 41-56

[56] S.D. Keegan, N.J. Mariani, O.M. Martínez, G.F. Barreto. **Behavior of catalytic pellets at high reaction rates. The effect of edges.** Ind. Eng. Chem. Res., 45 (2006), pp. 85-97

[57] K.B. Bischoff. **Accuracy of the pseudo steady state approximation for moving boundary diffusion problems.** Chem. Eng. Sci., 18 (1963), pp. 711-713

[58] D. Luss. **On the pseudo steady state approximation for gas solid reactions.** Can. J. Chem. Eng., 46 (1968), pp. 154-156

[59] G. Liu, S. Niksa. **Coal conversion submodels for design applications at elevated pressures. Part II. Char gasification.** Prog. Energy Combust. Sci., 30 (2004), pp. 679-717

[60] S. Halama, H. Spliethoff. **Numerical simulation of entrained flow gasification: reaction kinetics and char structure evolution.** Fuel Process. Technol., 138 (2015), pp. 314-324

[61] T. Dogu. **Diffusion and reaction in catalyst pellets with bidisperse pore size distribution.** Ind. Eng. Chem. Res., 37 (1998), pp. 2158-2171